Laboratory Testing of a Phase Induced Amplitude Apodization (PIAA) Coronagraph

Brian Kern*[a], Olivier Guyon[b], Amir Give'on[a], Andreas Kuhnert[a], Albert Niessner[a]
[a]Jet Propulsion Laboratory, California Institute of Technology,
4800 Oak Grove Dr., Pasadena, CA, USA 91109;
[b]The University of Arizona, Steward Observatory, Tucson, AZ USA 85721

ABSTRACT

We present high-contrast images from laboratory testing of a Phase Induced Amplitude Apodization (PIAA) coronagraph at NASA's High Contrast Imaging Testbed (HCIT). Using a deformable mirror and wavefront estimation and control algorithms, we create a "dark hole" in the monochromatic point-spread function with an inner working angle of 2.05 $f\lambda/D$, with a mean intensity 3.5×10^{-8}. We discuss the contributions to this floor, and the techniques being developed to improve it. We also present simulations that investigate the effect of Lyot stops of various sizes, and conclude that a Lyot stop is necessary for 10^{-9} performance but that an annular postapodizer is not necessary.

Keywords: Exoplanets, coronagraphy, deformable mirror, wavefront control, wavefront estimation

1. INTRODUCTION

1.1 PIAA coronagraph principle

This paper presents laboratory results from testing of a Phase Induced Amplitude Apodization (PIAA) coronagraph on the High Contrast Imaging Testbed (HCIT) at NASA's Jet Propulsion Laboratory. PIAA is a high-throughput, small inner-working angle, high spatial resolution coronagraphic technique proposed for space-based exoplanet imaging and spectroscopy missions[1-5]. To produce a stellar point-spread function (PSF) with a usable dark hole region with intensity at the 10^{-9} level, a deformable mirror (DM) is used to control the wavefront in the presence of diffraction and optical aberrations.

The effect of a pair of highly aspheric PIAA mirrors (M1 and M2) is called "remapping" and transforms a uniformly illuminated entrance pupil into an apodized pupil, as shown in Fig. 1. This is a lossless transformation, except for the mirror reflectances. The mirror shapes alone are not expected (even in the absence of aberrations) to produce a PSF with low sidelobes. In the traditional PIAA coronagraph architecture, an absorbing postapodizer is added (conjugated to M2), so that in the absence of aberrations, the PSF resulting from this apodized pupil has a wide region of 10^{-9} intensity (or another target level), normalized to its peak (see Fig. 1). For ease of fabrication, these postapodizers are typically specified as a series of opaque annuli, which are straightforward to fabricate as Al on glass, for example.

1.2 PIAA implementation on HCIT

The PIAA mirrors in this report were fabricated by Axsys, and are duplicates ("mirror images") of those described in Ref. 6. These are not the same mirrors as those previously used on HCIT, and described in Ref. 7, although they operate on the same PIAA principle.

The full coronagraph on HCIT uses several off-axis parabolas (OAPs) as relay optics. The PIAA M2 is conjugated to a postapodizer and again to the DM. The illumination of the DM covers approximately a 29-actuator diameter circle (out of 32×32 actuators). The light is brought to a focus where an occulter is located, then recollimated to pass through a Lyot stop, and imaged onto a CCD camera. A sketch of the layout is shown in Fig. 2.

Another effect of the remapping that apodizes the pupil amplitude is the distortion of the phase map of the input pupil. A tilted wavefront input on the PIAA mirrors produces a wavefront with much larger tilt in the center of the pupil where the amplitude is high, and a smaller tilt where the amplitude is low. This produces a magnification and aberration of off-

*Brian.D.Kern@jpl.nasa.gov; phone 1 818 395-6024; jpl.nasa.gov

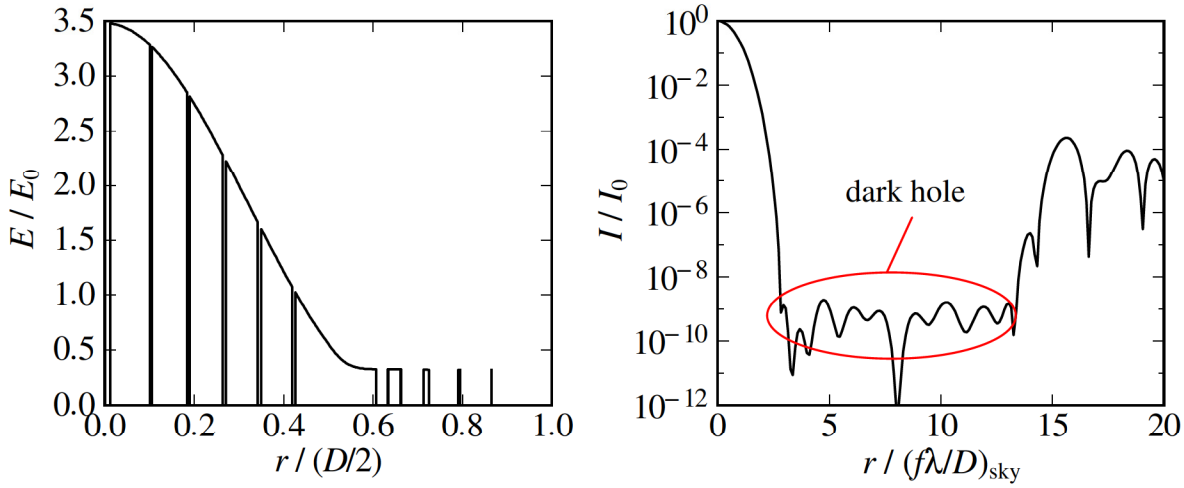

Fig. 1. (LEFT) Pupil-plane *E*-field radial distribution after PIAA remapping and annular postapodizer, and (RIGHT) resulting image-plane intensity. Both plots assume no wavefront aberrations.

axis sources, which depends on the postapodizer and Lyot stop. For the configuration described below, this magnification is 2.5. Locations referenced to a point in the source plane by dividing by this number are referenced by $(f\lambda/D)_{sky}$, where the "sky" subscript denotes corresponding locations in the source plane. The camera samples this resolution element with 5.8 pixels per $(f\lambda/D)_{sky}$.

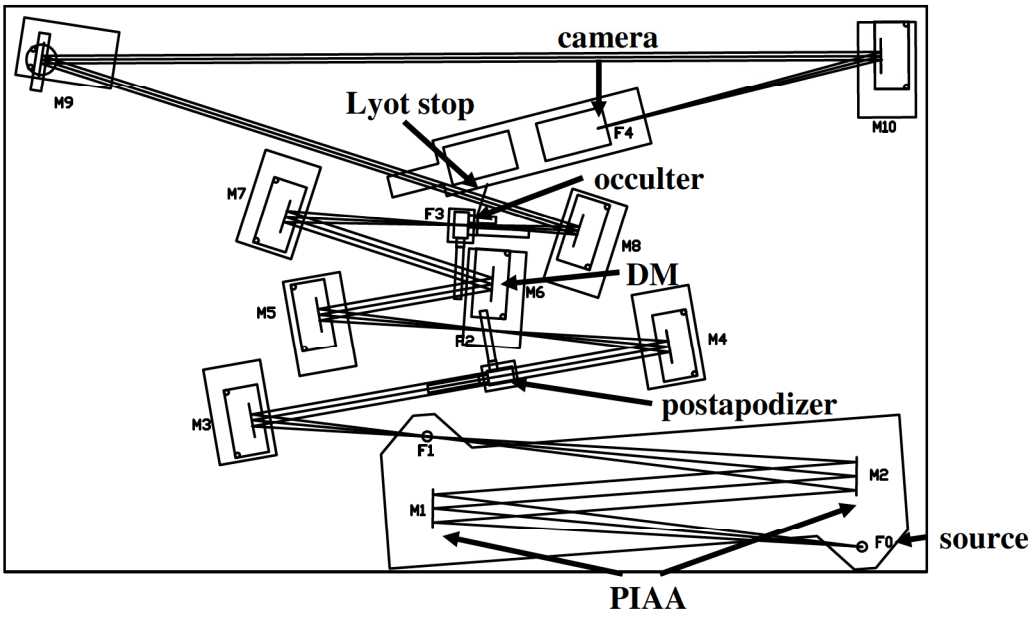

Fig. 2. Testbed optical layout. The outline is the edge of a 5×8-foot table located in a vacuum tank. The source is a 5 µm pinhole illuminated by a single-mode fiber (fed with light from outside the vacuum tank), labeled F0 at the bottom-right. The PIAA mirrors are M1 and M2, with M2 imaged onto a postapodizer between M3 and M4, then imaged onto a DM at M6. The occulter is at F3, with a Lyot stop between M8 and M9. The final image is at F4, which lands on a CCD, near the top.

The postapodizer used in this experiment is a simple circular stop (a traditional aperture), not an annular binary postapodizer as described above that is typically specified for PIAA coronagraphs. The motivation for this approach is described in detail below in Section 4.

2. WAVEFRONT CONTROL RESULTS

2.1 Intensity levels and morphology

The best results to date on this PIAA coronagraph, after wavefront control, demonstrate a dark hole mean intensity of 3.5×10^{-8}, with inner working angle 2.05 $(f\lambda/D)_{sky}$, as shown in Fig. 3. For comparison with planet detection considerations, the details of the shape of the 2-D area chosen as a dark hole can be reduced to first-order measures of intensity vs. radius, and area at that radius, as shown in Fig. 3. The azimuthal details of the dark hole are not particularly relevant, as long as the area is not divided so finely that a planetary image is likely to be disrupted by bright edges of the dark hole boundaries. As a relevant comparison to the area vs. radius plot, a nominal $(2\pi r\,\Delta r)/4$ line is shown; at each radius, this represents dark hole coverage of 1/4 of the 2π azimuthal range of a full field of view. Higher-order statistics (variance, min-max) as a function of radius are not presented here, but may be of interest for other investigations.

2.2 Uncontrollable light

Each iteration of wavefront control performed here requires an image-plane complex *E*-field estimate, to know what DM commands to send to reduce the dark hole intensity. This estimation process, described in Ref. 8, involves modulating the DM surface shape to systematically change the image-plane *E*-field in the dark hole, and taking an intensity image at each DM setting. This sequence of images (typically 5 images, one initial image and 4 "probe" images) can be analyzed analogously to having a phase-shifting interferometer at every pixel. This analysis produces an estimate of the real and imaginary parts of the image-plane *E*-field, as well as an uncontrollable intensity level, at each pixel. This uncontrollable intensity level is the analogy to incoherent light in a phase-shifting interferometer, *i.e.*, it does not respond

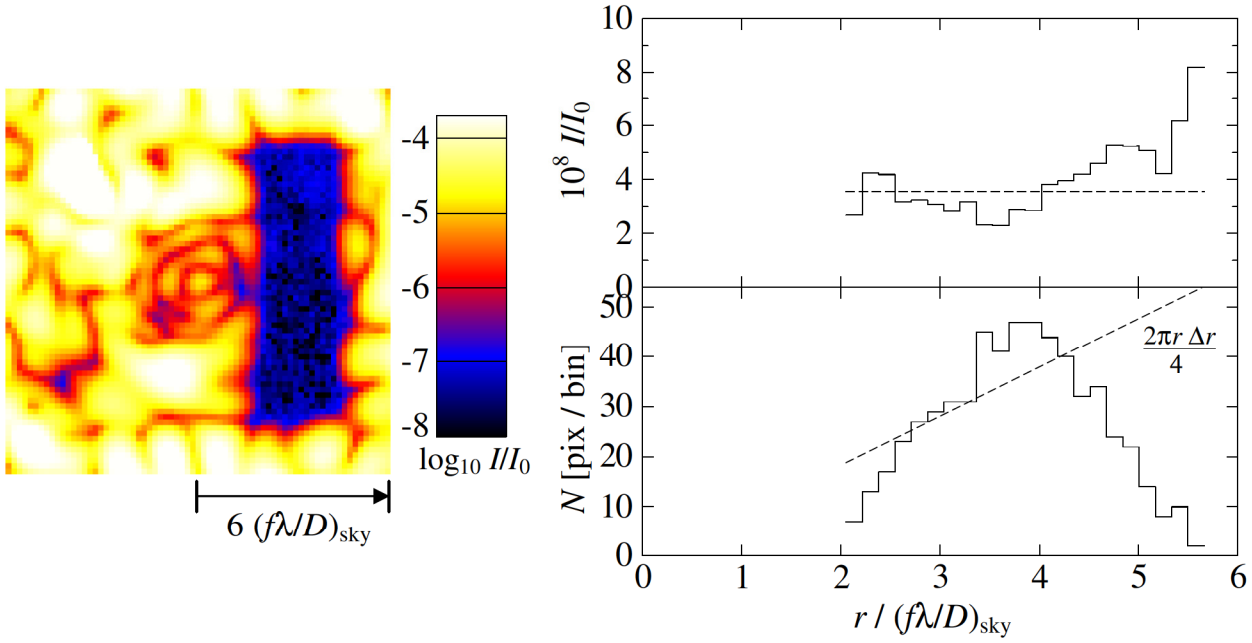

Fig. 3. (LEFT) Normalized intensity, (TOP RIGHT) mean dark hole intensity vs. radius, and (BOTTOM RIGHT) dark hole area vs. radius. I_0 is the unocculted star peak intensity. The dashed line in the top right panel is the mean intensity over the entire dark hole, 3.5×10^{-8}. The dashed line in the bottom right panel is a nominal area corresponding to 1/4 of a full 2π azimuthal coverage at each radius.

to modulation of the phase of the probe *E*-field.

The results presented here are dominated by uncontrollable light, as determined by the wavefront estimation process. Any improvements to the dark hole intensity will come not from further wavefront control, but rather by changes to the coronagraph architecture or environment. The attempt to identify and mitigate these issues is described in the next section.

3. INVESTIGATIONS INTO CONTRAST LIMITS

3.1 Sources of uncontrollable light

The conditions under which light can appear to be uncontrollable (DM modulation does not have an interferometric signature on intensities) can be categorized as insufficient resolution in a number of ways:

1. Spatially unresolved – feature sizes are smaller than camera pixel Nyquist sampling
2. Temporally unresolved – conditions evolve faster than the sequence of camera images
3. Spectrally unresolved – OPDs exceed coherence length of source, "incoherent" light
4. Unresolved polarization states – mutually orthogonal polarization states will not interfere
5. Measurement noise

The measurement of uncontrollable light can be a result of noise, whether random or systematic. Random noise will tend to result in a reduced measurement of uncontrollable light (*i.e.*, it will overestimate modulation). Systematic noise sources, such as poor dark subtraction, can certainly contribute to a measurement of uncontrollable light. All measurements presented here have been dark-subtracted, where dark frames at different exposure times are taken without opening the shutter on the light source (located outside of the vacuum tank). This dark subtraction will accommodate detector-specific contributions (*e.g.*, thermal dark current) as well as light sources internal to the vacuum tank (encoders on motors).

Specific examples of mechanisms that would produce uncontrollable light would be vibrations at temporal freqnecies of Hz and above (the science camera has a 7 s readout cycle), ghosts landing on the camera with large wavefront tilts w.r.t. the direct wavefront (spatially unresolved fringes), ghosts that have a large OPD w.r.t. the direct wavefront (partially coherent, depending on the source coherence length), or ghosts with modest OPDs and a source spectrum that is narrowband but temporally variable.

3.2 Experiments with uncontrollable light

A number of potential mechanisms for producing uncontrollable light have been investigated, either in simulations or by changes to the testbed. The net effect of these investigations was to go from a mean contrast of 4×10^{-7}, dominated by uncontrollable light, to 3×10^{-8}, also dominated by uncontrollable light. The dominant improvements were the introductions of a pinhole at the source (spatially filtering what had been a bare fiber tip), a linear polarizer, and a Lyot stop. A table of investigations is shown in Table 1. In many cases, the limits are loose upper limits.

The priorities for upcoming investigations are first to handle image motion (discussed in the following subsection), then to introduce a more restrictive occulter (blocking more light that could produce ghosts), and add (and rotate) a second linear polarizer.

3.3 Analysis of image motion

An ongoing investigation is the extent to which image motion, *i.e.*, pupil plane phase tip/tilt, plays a role in all contrast issues. There are two modes of image motion that are relevant: motion upstream of the PIAA remapping and motion downstream. Motion upstream of the PIAA remapping will result in a distorted tip/tilt phase representation after the PIAA remapping, which cannot be corrected entirely by applying tip/tilt downstream of PIAA. Motion downstream of the PIAA remapping can be corrected by tip/tilt downstream of PIAA, but not entirely by correcting tip/tilt upstream of PIAA. The image motion observed is on the order of 0.5-1 μm at the occulter for timescales up to several 10s of seconds, but the identification of what portion of that motion is occurring upstream vs. downstream of PIAA has not been completed.

Table 1. Physical sources for uncontrollable light limits

Origin	Mechanism	Test	$\log_{10}$ limit
Poor occulter image	Finite optics / truncation	Add Lyot stop	-8
	Scattering	Add Lyot stop	-8
Temporal variability	Low freq drift	Repeat unchanged	< -7
	High freq vibration	Low-order wavefront sensor	< -7
Fiber / pinhole as source	Source wavefront morphology	Add / change pinhole	< -8
Camera pixel size	Misinterpret DM probes	Numerical analysis	< -9
Ghosts	OPD by glass/air reflect, CCD, source partially incoherent	Move optics / occ	?
Scattered light	Poor baffling	Add baffling	?
Polarization	Incoherent states at source	Add / change pinhole	< -8
	Ghost with altered pol. State	Move optics / occ	-8?

If there were no Lyot stop in the system, motion downstream of PIAA would have almost no effect on dark hole intensities. However, with a Lyot stop, motion both upstream and downstream have a significant effect on intensities throughout the dark hole. Depending on several other factors, this 0.5-1 μm scale of image motion may be responsible for anywhere from 5×10^{-9} to 3×10^{-8} mean intensity across the dark hole.

Because this factor alone could account for much of the 3.5×10^{-8} mean intensity seen, accommodating this image motion is the highest priority for improvements in performance. A low-order wavefront sensor and actuators are being installed on the PIAA coronagraph, with actuators for tip/tilt of the DM (downstream) and the introduction of an actuated fold mirror between the source and PIAA M1 (upstream). This low-order system is substantially similar to that described in Ref. 9. A sketch of the optical layout including the low-order system is shown in Fig. 4. The low-order camera used here (separate from the science camera observing the coronagraphic images) is a 50 Hz CCD camera, although the bandwidth used in testing has been 2 Hz. Initial tests have identified a f^{-2} power law in the image motion temporal frequency power spectrum, extending from at least mHz to a few Hz (all that was used in the early data analysis). Since the science camera operates typically at ~ tens to 100 mHz frequencies, most of the relevant power is likely in the sub-Hz regime.

4. LYOT STOP AND POSTAPODIZER ARCHITECTURAL CONSIDERATIONS

4.1 Use of Lyot stop and postapodizer

The original PIAA coronagraph architecture does not use a Lyot stop. In the baseline PIAA configuration, with no wavefront aberrations, the PIAA mirror remapping and a postapodizer create a dark hole at the image plane, with no need for further optics to reduce light in the dark hole. An occulter can be added to this configuration simply to reduce the dynamic range of the image landing on the camera by blocking the uninteresting bright core of the star – the occulter is imaged onto the camera, and simply avoids having light hit the detector pixels where the occulter blocks it. This occulter setup does not then affect the brightness of a dark hole; the occulter transmission has a purely local effect on the image.

The presence of a Lyot stop between the occulter and the camera causes the light that passes the occulter to spread throughout the image plane; the camera no longer sees an exact duplicate of the occulter plane. In the case of a perfect wavefront, if the occulter blocks all of the bright light, the addition of a mild Lyot stop produces a small reduction in spatial resolution, and a small loss of throughput (because little light is present near the edge of the pupil), but its presence or absence is of little concern.

In the presence of wavefront aberrations, the situation is more complicated. With modest wavefront aberrations, the spatial frequency components of the wavefront errors (measured after the PIAA remapping) correspond directly to the brightness of locations in the image plane, regardless of the state of the postapodizer (*i.e.*, present or not). Specifically,

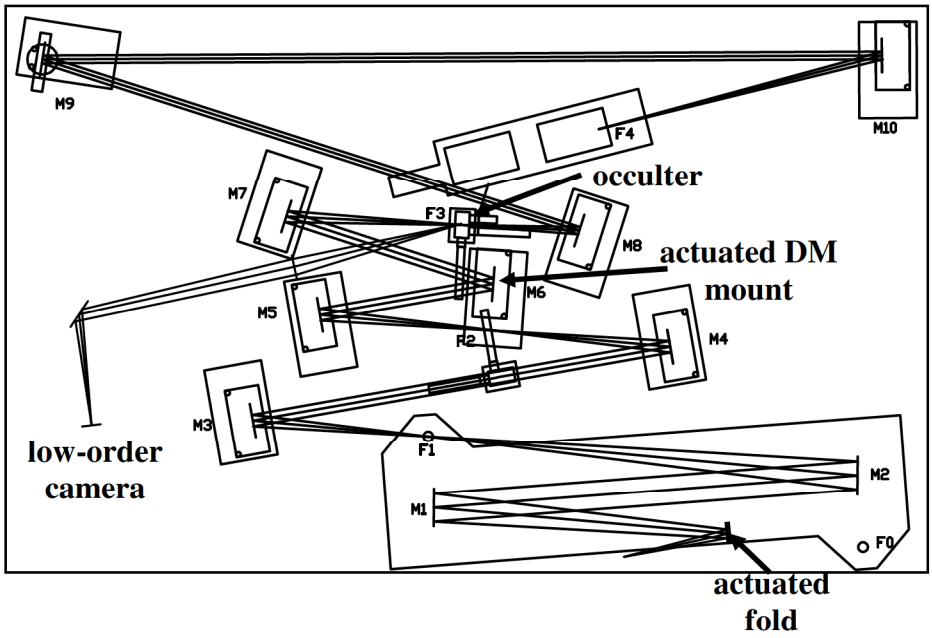

Fig. 4. Upgrades to testbed to enable low-order wavefront sensing and control. Piezo actuators were added to the DM mount to allow tip/tilt control downstream of PIAA, and a fold was introduced near the source (at bottom-right) with piezo actuators to allow tip/tilt control upstream of PIAA. The reflected light off the occulter is imaged onto the low-order camera, then control signals are sent to the tip/tilt controls both upstream and downstream.

if the postapodizer is designed to deliver a 10^{-10} intensity in the dark hole, but the optics themselves produce 10^{-5} aberrations, the details of the postapodizer design will not be relevant in the dark hole before wavefront control.

The interaction between the postapodizer and wavefront control is best investigated using wavefront control simulations. Similarly, the choice of Lyot stop has relatively little effect before wavefront control, but can be investigated through simulations.

4.2 Simulated contrast behavior of different Lyot sizes and postapodizer choices

To simulate this testbed appropriately, the phase and amplitude of the exit pupil of the real system, with no postapodizer, are first estimated. This is done using the phase retrieval method described in Ref. 7. For the data analyzed here, the phase estimation had been performed and the DM adjusted to make the flattest phase map possible, over several iterations of phase retrieval and DM actuation. The DM shape at the end of "flattening" is the "zero-point" for all further DM motions. These phase and amplitude estimates of the flattened wavefront provide the starting point for all simulations, and are shown in Fig. 5. No individual optical aberrations are represented separately from the system exit pupil wavefront. The simulations are monochromatic at 808 nm (the wavelength used to estimate the exit pupil amplitude and phase), using a single 32×32-actuator DM. The dark holes created are essentially the same location and shape as that described in the real testbed results above. Only mean intensity over the entire region is considered here, not the distribution of that intensity over the dark hole area.

The simulations are carried out using EFC as described in Ref. 10. EFC is an iterative linearization of the relationship between actuator positions and image-plane *E*-field (which is inherently nonlinear), and in these simulations, the Jacobian representing that linearization is recalculated every iteration. This Jacobian recalculation is a way to minimize the total number of iterations to reach a desired contrast level.

Choosing 10^{-9} as a target contrast, several metrics may be considered as methods of determining the "best" architecture configuration. The metrics proposed here are the number of iterations to reach 10^{-9}, and the rms DM displacements required to reach 10^{-9}. We do not consider final contrast at the end of 20 iterations to be an appropriate metric for this investigation, as the details of the contrast limits at the 10^{-11} level are not relevant to a 10^{-9} testbed goal. The number of iterations metric benefits by having a direct practical utility in terms of real-world testbed expectations, but is a bit

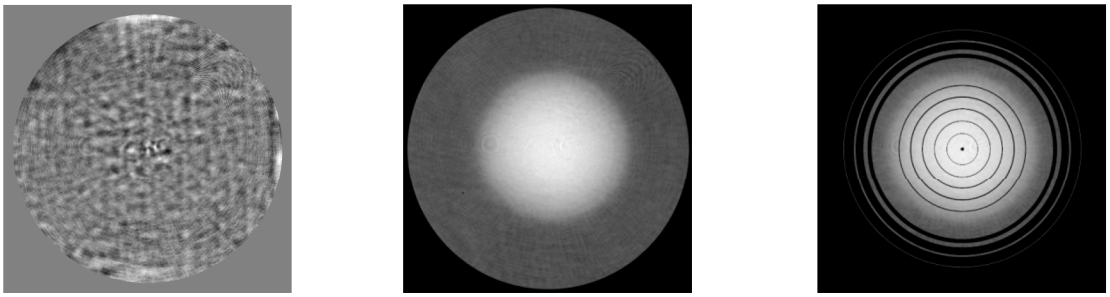

Fig. 5. (LEFT) Estimated phase, (CENTER) estimated amplitude, and (RIGHT) estimated amplitude with annular postapodizer applied, seen through the entire coronagraph with no occulter. The phase map is displayed on a linear scale from −1 to +1 radian, the two amplitude maps are log-scaled with arbitrary normalization. The amplitude at the edge is approximately 1/10 that at the center. The log scaling of the amplitude hides some large (+/− 20%) high spatial frequency amplitude aberrations near the center. This phase had been flattened by iterative phase estimation and DM adjustments before the data shown here were taken. The residual wavefront phase shown here is at spatial frequencies or positions beyond the control of the DM; the residual rectilinear features are DM surface features.

ambiguous in that, in simulations with perfect knowledge, the number of iterations is primarily a measure of the nonlinearity of the relationship between actuator motions and image plane *E*-field. Whether or not this is a relevant concern for testbed limitations is unclear.

The testbed simulations are run first with an annular binary postapodizer designed to give a 10^{-9} dark hole, using 10 annuli. The appearance of this postapodizer is shown in the right panel of Fig. 5. A range of Lyot stop sizes is used, as well as no Lyot stop. For each Lyot stop size, 20 iterations are calculated. A plot of the number of iterations required to reach 10^{-9} is shown in the left panel of Fig. 6, and a plot of the rms DM displacements required in the left panel of Fig. 7. Then the same set of Lyot sizes are simulated with only a circular stop postapodizer (*i.e.*, the system pupil stop), and the results are plotted in the right panels of Figs. 6 and 7.

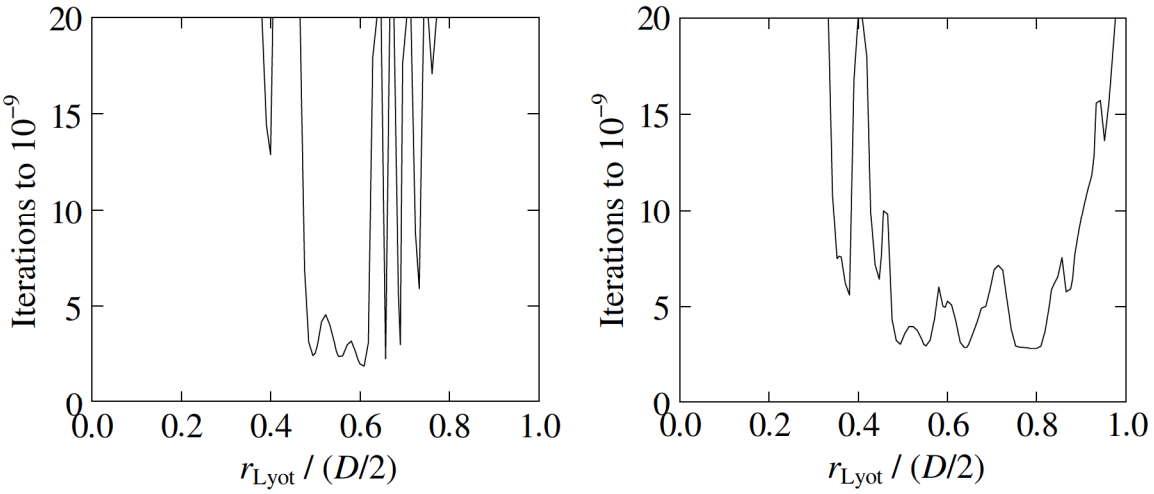

Fig. 6. Number of iterations for simulation to reach 10^{-9} mean dark hole intensity vs. Lyot stop radius, for (LEFT) annular binary postapodizer, and (RIGHT) circular stop postapodizer (*i.e.*, no postapodizer). Many radii did not reach 10^{-9} in 20 iterations. The mean intensity for no Lyot stop (not shown on the plots) with the annular postapodizer was 7×10^{-9}, for the circular stop was 10^{-8}. For the annular postapodizer, many of the sharp "spikes" in number of iterations correspond to the locations of edges of the annuli.

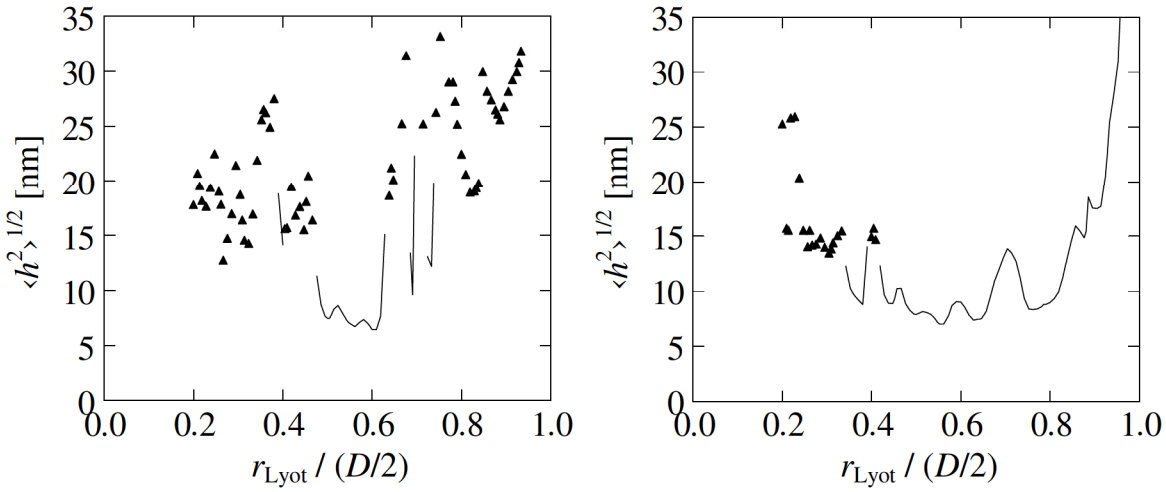

Fig. 7. rms actuator displacements required for simulation to reach 10^{-9} mean dark hole intensity vs. Lyot stop radius, for (LEFT) annular binary postapodizer, and (RIGHT) circular stop postapodizer (*i.e.*, no postapodizer). The ‹…› denotes a mean over the actuators visible out to the system diameter D. Triangles denote lower limits, for cases where the contrast did not reach 10^{-9} in 20 iterations.

Many configurations did not reach 10^{-9} in 20 iterations. Notably, the case of no Lyot stop at all produced dark hole mean intensities of 7×10^{-9} and 10^{-8} for the annular postapodizer and circular postapodizers. These intensities can be compared to the mean intensity at the end of 20 iterations for a "good" Lyot stop size, which came to 10^{-11} in many cases (for the circular postapodizer in particular).

Coupled with any consideration of the dark hole intensity performance must be an efficiency analysis. Because the PIAA remapping leaves such a low surface brightness to the outer half of the pupil, the throughput loss is very mild as that light is removed. A plot of Lyot throughput versus Lyot radius is shown in Fig. 8. The case of $r_{\mathrm{Lyot}} = 0.55$ (D/2), which was used on the testbed for the results presented here, has a Lyot throughput of 0.94. For similar reasons (low brightness at the edge of the pupil), the loss of angular resolution is very mild for the attractive Lyot stop radii.

4.3 Conclusions regarding Lyot stop and postapodizer

Examining Figs. 6 and 7, it is apparent that for an appropriate choice of Lyot stop size, the presence of an annular postapodizer provides little benefit. Specifically, the number of iterations to reach 10^{-9} is very similar for the best Lyot stop size in each case (2-3 iterations), and the rms DM displacements to reach 10^{-9} are also very similar (6-7 nm rms).

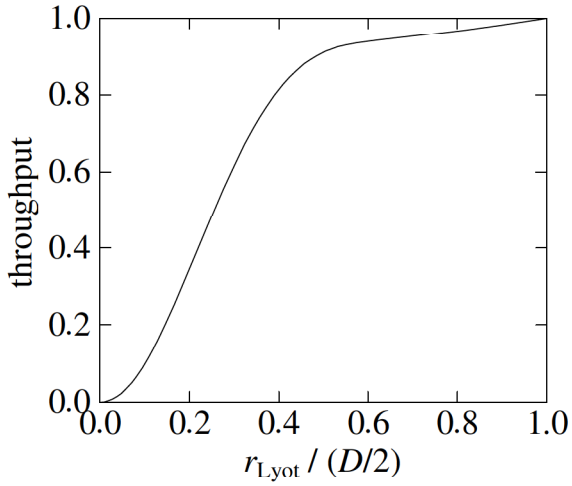

Fig. 8. Throughput of Lyot stop vs. Lyot stop radius.

The current realizations of annular postapodizers involve glass substrates, which introduce some level of ghost reflections. Given these considerations, this experiment should be able to proceed without an annular postapodizer, that is, using only the system circular stop, and expect to reach a similar dark hole intensity as expected from using an annular postapodizer.

A strong caveat to the conclusion that the annular binary postapodizer provides little benefit is that these simulations were monochromatic. It remains to be seen if there is an advantage to an annular postapodizer in a broadband situation.

A final note of unresolved mystery is that empirically, the inclusion of a modest-sized Lyot stop reduced the uncontrollable light floor. By construction, that empirical result has no representation in the simulations presented here; in these simulations, all of the light is controllable. There then seem to be two benefits of Lyot stops: their coordination with wavefront control, and their reduction of uncontrollable light.

5. SUMMARY

The mechanisms that currently limit the performance of the PIAA coronagraph on HCIT have not yet been identified. A low-order wavefront correction system is currently being installed on the table, which should answer the highest priority question regarding the contrast limits, that of image motion. A short list of other investigations will follow, preparations for which are currently under way.

We have identified the utility of a Lyot stop in assisting wavefront control, and not found any additional benefit to an annular binary postapodizer when used with a Lyot stop and wavefront control.

ACKNOWLEDGEMENTS

Continued discussions with Ruslan Belikov, Dwight Moody, and John Trauger have greatly benefited this investigation. In particular, John Trauger secured funding and procured the equipment (table, mounts, stages, and OAPs) that currently make up the bulk of the PIAA coronagraph. Frantz Martinache has been particularly valuable in the early implementation of the low-order wavefront sensor and control.

The research described in this publication was carried out at the Jet Propulsion Laboratory, California Institute of Technology, under a contract with the National Aeronautics and Space Administration.

REFERENCES

[1] Guyon, O. et al., "The pupil mapping exoplanet coronagraphic observer (PECO)," Proc. SPIE 7731, 773129 (2010).
[2] Trauger, J. et al., "ACCESS: a concept study for the direct imaging and spectroscopy of exoplanetary systems," Proc. SPIE 7731, 773128 (2010).
[3] Guyon, O. et al., "Exoplanet imaging with a phase-induced amplitude apodization coronagraph. I. Principle," Astrophys. J. 622, 744-758 (2005).
[4] Vanderbei, R.J., Traub, W.A., "Pupil mapping in two dimensions for high-contrast imaging," Astrophys. J. 626, 1079-1090 (2005).
[5] Guyon, O. et al., "Theoretical limits on extrasolar terrestrial planet detection with coronagraphs," Astrophys. J. Supp. Series 167, 81-99 (2006).
[6] Guyon, O et al., "High-Contrast Imaging and Wavefront Control with a PIAA Coronagraph: Laboratory System Validation," Pub. Astron. Soc. Pacific 122, 71-84 (2010).
[7] Kern, B. et al., "Phase-induced amplitude apodization (PIAA) coronagraph testing at the High Contrast Imaging Testbed," Proc. SPIE 7440, 74400H (2009).
[8] Give'on, A., Shaklan, S., Kern, B., "Pair-wise, image plane-based electric field estimation for high-contrast coronagraphy," Proc. SPIE 8151-35 (this proceedings) (2011).
[9] Guyon, O., Matsuo, T., Angel, R., "CORONAGRAPHIC LOW-ORDER WAVE-FRONT SENSOR: PRINCIPLE AND APPLICATION TO A PHASE-INDUCED AMPLITUDE CORONAGRAPH," Astrophys. J. 693, 75-84 (2009).
[10] Give'on, A., Kern, B., Shaklan, S., Moody, D.C., Pueyo, L., "Broadband wavefront correction algorithm for high-contrast imaging systems," Proc. SPIE 6691, 66910A (2007).